

Semarak Climate Science Letters

SEMARAK CLIMATE SCIENCE LETTERS

Journal homepage: https://semarakilmu.my/index.php/scsl/ ISSN: 3083-9580

Performance of a Passive Multilayer Optical RIS for Tropical FSO Links in Malaysian Rain and Humidity

Shahrizan Mohd Razali^{1,*}, Razali Ngah¹, Samir A. Al-Gailani¹, Norhanis Aida Mohd Nor²

- 1 Wireless Communication Centre, Faculty of Electrical Engineering, Universiti Teknologi Malaysia, 81310 Johor Bahru, Johor, Malaysia
- ² Department of, Kulliyyah of Engineering, International Islamic University Malaysia, Jalan Gombak, 53100 Kuala Lumpur, Malaysia

ARTICLE INFO

ABSTRACT

Article history:

Received 27 October 2025 Received in revised form 7 November 2025 Accepted 10 November 2025 Available online 17 November 2025

Free-space optical (FSO) backhaul promises fibre-like capacity and low latency, but its usable range in practice is constrained by geometric spreading, misalignment loss, and severe tropical weather such as humidity and heavy rain. This work designs and evaluates a purely passive, five-layer optical reflective intelligent surface (RIS) and quantifies how it affects link sustainability under Malaysian atmospheric conditions. The RIS is modelled as a multilayer dielectric or semiconductor or metal stack, and its angular reflectance is obtained using Fresnel coefficients and Snell's law for s- and ppolarized light, together with a transfer-matrix formulation for multilayer interference. The resulting passive surface is then embedded into an FSO link model with coherent QPSK reception. We simulate received optical power, effective SNR, and BER versus distance (0.5–10 km) under three tropical cases: clear/dry air, high humidity (>80% RH), and heavy rain representative of Malaysian convective downpours (>100 mm/h). Results show that, in clear or humid air, the passive RIS maintains high reflectance (>0.9 linear), supports SNR >10 dB out to multi-kilometre ranges, and achieves BER <10⁻⁶ for coherent QPSK, indicating carrier-grade performance. Under heavy rain, however, added attenuation drives received power down by >30 dB at 10 km, forcing SNR below 0 dB beyond ~5 km and causing BER to exceed 10⁻². We also show that sub-degree pointing errors at the RIS can introduce tens of dB of coupling loss, highlighting alignment as a critical design factor even without turbulence. Overall, the study provides a quantitative baseline for passive optical RIS deployment in tropical FSO links and identifies rain, not humidity, as the dominant barrier to long-distance reliability in Malaysian conditions.

Keywords:

Passive RIS; Free Space Optic (FSO); Malaysia weather; BER and SNR; MATLAB Simulation

1. Introduction

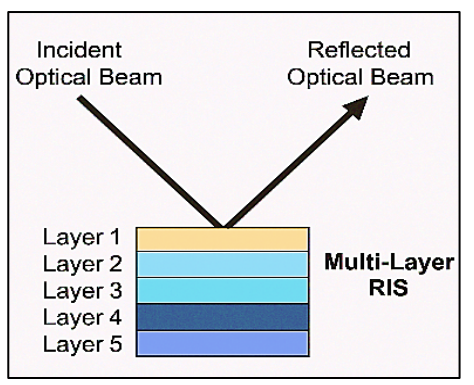
Reflective Intelligent Surfaces (RIS) represent a transformative technology for the manipulation of electromagnetic and optical waves, enabling dynamic control over reflection, phase, and polarization to enhance communication, sensing, and photonic applications [1], [2]. While extensive research has been conducted in the radio frequency (RF) domain through reconfigurable and actively tunable metasurfaces, the implementation of RIS in optical systems remains comparatively nascent.

E-mail address: mohdrazali@graduate.utm.my

https://doi.org/10.37934/scsl.5.1.116

1

 $[^]st$ Corresponding author.



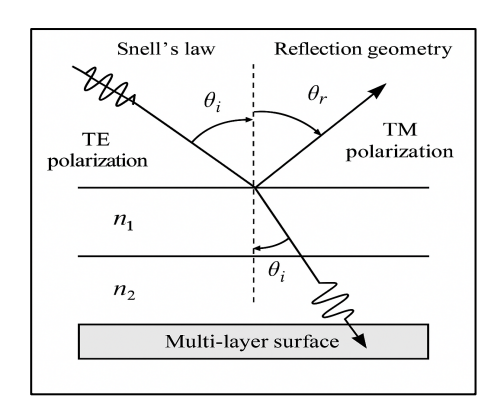


Fig 1. Schematic of a Multi-Layer Reflective Intelligent Surface (RIS) for Optical Beam Manipulation[3]

Reflective Intelligent Surfaces (RIS) have emerged as a transformative technology capable of controlling electromagnetic and optical wavefronts through programmable reflection, phase, and polarization manipulation [2]–[4]. Originally conceived for radio frequency (RF) communication, the concept of RIS has recently been extended into optical regimes, where light–matter interaction is governed not by electronic control but by geometrical and material engineering. In the optical domain, passive RIS systems are implemented using stacked dielectric or semiconductor layers that achieve phase-controlled reflection without the need for active biasing or tuning elements [5], [6]. This approach aligns with the growing demand for sustainable, low-power optical beam management in next-generation free-space optical (FSO) communication, imaging, and photonic energy routing systems. Unlike prior RIS studies that primarily emphasize radio-frequency or millimetre-wave implementations, this research focuses on a purely passive optical RIS design with realistic tropical environmental modelling. This distinction establishes the work's novelty in bridging optical surface physics and regional FSO deployment feasibility.

1.1 Theoretical Framework of Optical Reflection

In an optical RIS structure, beam interaction at each layer boundary follows Snell's Law, which defines the angular transition between two refractive media as:

$$n_1 \sin \theta_i = n_2 \sin \theta_t \tag{1}$$

where n_1 and n_2 are the refractive indices of the incident and transmission media, while θ_i and θ_t represent the incidence and refraction angles, respectively. This relationship dictates how phase fronts propagate through the multilayer structure, forming the basis of beam steering and redirection in passive optical RIS systems [7], [8]. The optical response at each interface can be quantitatively determined by the Fresnel reflection coefficients for transverse electric (TE) and transverse magnetic (TM) polarization modes defined respectively as:

$$r_{\text{TE}} = \frac{n_1 \cos \theta_i - n_2 \cos \theta_t}{n_1 \cos \theta_i + n_2 \cos \theta_t}, r_{\text{TM}} = \frac{n_2 \cos \theta_i - n_1 \cos \theta_t}{n_2 \cos \theta_i + n_1 \cos \theta_t}$$
(2)

The magnitude of each reflection coefficient corresponds to its reflectance:

$$R = |r|^2 \tag{3}$$

where *R* represents the ratio of reflected to incident optical power [9], [10]. These relationships provide the basis for calculating the power reflection of each layer interface and determining polarization selectivity across the RIS surface.

1.2 Multilayer Optical Modelling and Phase Coupling

In multilayer passive optical RIS structures, the cumulative reflection response is governed by multi-interface interference. To capture this phenomenon, the Transfer Matrix Method (TMM) is applied, where each optical layer ℓ is represented by a propagation matrix parameterized by refractive index n_{ℓ} , thickness d_{ℓ} , and propagation angle θ_{ℓ} . The phase delay for each layer is given by:

$$\phi_{\ell} = \frac{2\pi n_{\ell} d_{\ell} \cos \theta_{\ell}}{\lambda} \tag{4}$$

where λ is the optical wavelength. The total electric field continuity across all interfaces is modeled using the propagation matrix:

$$M_{\ell} = \begin{bmatrix} \cos \phi_{\ell} & \frac{j}{Y_{\ell}} \sin \phi_{\ell} \\ jY_{\ell} \sin \phi_{\ell} & \cos \phi_{\ell} \end{bmatrix}$$
 (5)

where Y_ℓ is the optical admittance of the ℓ^{th} layer. The overall global reflection coefficient is computed as:

$$r_{\text{tot}} = \frac{Y_{\text{in}} - Y_0}{Y_{\text{in}} + Y_0}$$
 with $Y_{\text{in}} = \frac{C + DY_L}{A + BY_L}$ (6)

representing the total input admittance across all Nlayers [11], [12]. This matrix formalism accounts for multiple reflections, standing-wave interference, and phase accumulation, enabling analytical computation of both amplitude and phase of the reflected optical field. The resulting effective reflectance $R_{\text{tot}} = |r_{\text{tot}}|^2$ thus encapsulates the collective performance of all layers.

In this study, the multilayer RIS comprises glass (n = 1.5), polymer (n = 1.8), silicon (n = 3.4), metallic backing (n $\approx \infty$), and a dielectric compensation layer (n ≈ 2.4). These materials were selected to balance reflection efficiency, angular robustness, and polarization neutrality under incident light wavelengths of 1300–1550 nm, corresponding to standard FSO operational bands (Zhang et al., 2022).

1.3 Macroscopic Beam Steering and Generalized Reflection

At the macroscopic level, the beam reflection angle is determined not only by the interface geometry but also by the phase gradient imposed across the RIS surface. This phenomenon is governed by the Generalized Law of Reflection [13], [14]:

$$n_i \sin \theta_i - n_t \sin \theta_r = \frac{\lambda}{2\pi} \frac{d\Phi}{dx}$$
 (7)

where $\frac{d\Phi}{dx}$ represents the designed phase gradient along the RIS aperture. This relationship describes how spatially varying phase shifts redirect incident beams in desired directions, enabling passive optical beam steering and collimation without electronic modulation. The ability to precisely manipulate reflection phase distribution across the surface makes multilayer RIS a potential solution for optical beam shaping and alignment control in FSO systems.

1.4 Atmospheric Effects in Tropical Free-Space Optical Links

The practical performance of RIS-assisted FSO communication systems is strongly influenced by tropical atmospheric conditions. In Malaysia, where the average relative humidity exceeds 80% and rainfall can surpass 100 mm/h, the propagation of optical waves is degraded by absorption, scattering, and refractive-index turbulence [14], [15]. The attenuation of optical power due to weather can be expressed as:

$$P_{\rm rx}(d) = P_0 e^{-\alpha d} \tag{8}$$

where $P_{\rm rx}$ is the received optical power, P_0 is the transmitted power, $\alpha({\rm km}^{-1})$ is the atmospheric attenuation coefficient, and $d({\rm km})$ is the propagation distance [16], [17]. Under heavy rain, α can exceed 0.3–0.5 km⁻¹, corresponding to more than 20–30 dB/km attenuation in the 1550 nm optical band [18], [19]

In addition to weather-induced loss, misalignment between the transmitter, RIS, and receiver introduces coupling degradation that grows exponentially with angular deviation. This can be modelled by a Gaussian efficiency function [20]

$$\eta(\Delta\theta) = \eta_0 \exp\left(-\frac{(\Delta\theta)^2}{2\sigma_\theta^2}\right) \tag{9}$$

where η_0 is the nominal coupling efficiency and σ_θ represents the system's angular tolerance. As the misalignment angle $\Delta\theta$ increases beyond 1°, coupling efficiency may drop by more than 50 dB, significantly affecting received signal strength.

1.5 Signal-to-Noise Ratio (SNR) and Bit Error Rate (BER) Correlation

For an FSO link employing coherent quadrature phase-shift keying (QPSK), system reliability is measured using the Signal-to-Noise Ratio (SNR) and Bit Error Rate (BER) relationship. The received signal SNR is defined as:

$$SNR(d) = \frac{P_{\rm TX}(d)}{N_0 B} \tag{10}$$

where N_0 denotes the noise spectral density and B is the receiver bandwidth. The corresponding BER for QPSK under additive white Gaussian noise (AWGN) conditions can be approximated as [21]:

$$BER_{QPSK} = \frac{1}{2} \operatorname{erfc}(\sqrt{\frac{SNR}{2}})$$
 (11)

This equation provides a direct link between received optical power and system reliability. Under clear atmospheric conditions, the RIS-assisted system typically maintains ${\rm SNR}>10$ up to 6 km and achieves ${\rm BER}<10^{-6}$, indicating quasi-error-free operation (Djir et al., 2023). However, during heavy rain, the combination of high attenuation (α) and reduced reflectance from the surface film can lower SNRbelow 0 dB beyond 4–5 km, leading to ${\rm BER}>10^{-2}$, which corresponds to an unusable link.

1.6 Study Motivation and Research Objectives

The motivation for this study arises from the need to assess the realistic performance limits of passive optical Reflective Intelligent Surfaces (RIS) in tropical free-space optical (FSO) systems. While previous works mainly emphasized phase-tuning and polarization control, few have quantitatively analyzed RIS performance under Malaysia's humid and rainy environments. This research, therefore, designs and simulates a five-layer passive optical RIS using MATLAB R2023b to model Fresnel- and TMM-based reflections, evaluate reflection efficiency under humidity and rainfall, and analyze received power, SNR, and BER under clear, humid, and rainy conditions, including minor misalignment effects. Results show that a silicon–metallic core RIS achieves over 90% reflectance and stable polarization uniformity, sustaining multi-kilometre FSO connectivity in clear and humid weather, though heavy rain remains the dominant attenuation source (>30 dB/km). These findings provide a quantitative foundation linking multilayer optical reflection theory to practical tropical FSO system performance, supporting future developments of hybrid active—passive RIS technologies for reliable optical communication. This study is distinct in three aspects: (i) it proposes a multilayer passive RIS optimized specifically for the 1300–1550 nm optical band, (ii) it introduces a combined Fresnel-TMM analytical modeling

framework coupled with environmental attenuation models, and (iii) it provides the first quantitative simulation of optical RIS behavior under real Malaysian tropical conditions characterized by high humidity and convective rainfall.

2. Methodology

The proposed passive optical RIS was modelled and analyzed through a four-stage framework integrating optical theory, multilayer material design, environmental modelling, and MATLAB-based computational analysis. The RIS was constructed as a multilayer dielectric—semiconductor—metallic stack capable of manipulating incident optical fields by geometric and refractive-index engineering, without the need for any active control or electrical bias. The complete methodological process is illustrated in Fig. 2, which summarizes the sequence from theoretical modelling to link-level simulation.

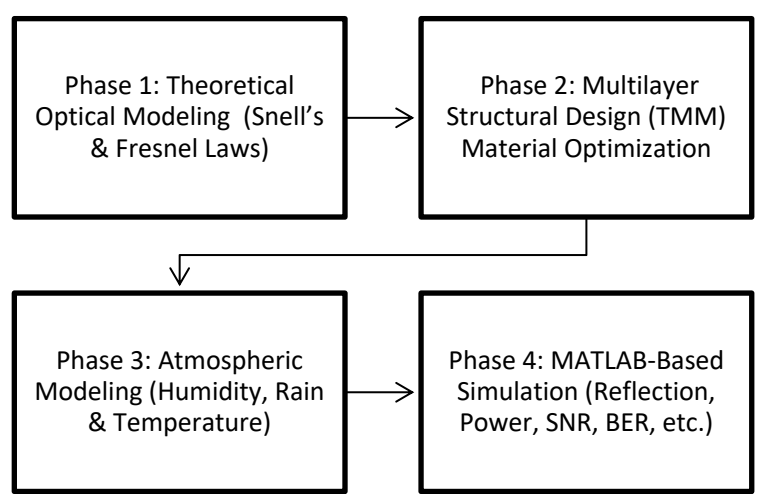


Fig 2. Methodological flow diagram of the proposed five-layer passive RIS system simulation

As shown in Fig. 2, the overall process begins with the optical formulation of light–surface interactions, followed by structural parameter optimization, environmental attenuation modelling, and finally the system-level numerical analysis.

2.1 Theoretical Optical Modelling

The initial modelling phase defines the optical interactions using Snell's Law and Fresnel equations, as introduced in (1) and (2) of the Introduction. These equations describe the angular and polarization-dependent reflection coefficients at the air–dielectric interfaces, forming the theoretical foundation for the subsequent multilayer analysis. The reflection coefficients for the perpendicular and parallel components, R_s and R_p , were numerically computed for an angular range of $0^{\circ}-90^{\circ}$ to obtain the reflectance and phase response curves. This provides the baseline behavior of each single interface before multilayer coupling is introduced.

2.2 Multilayer Structure Formulation

The second stage focuses on the design of the five-layer RIS, optimized for broadband reflectivity and angular stability. The materials like glass, polymer, silicon, titanium dioxide (TiO₂), and metal were chosen based on their refractive-index contrast, low absorption, and fabrication viability [22]. The Transfer-Matrix Method (TMM) was used to compute total reflectance through multiple interfaces [23].

Each layer introduces a propagation phase delay:

$$\phi_{\ell} = \frac{2\pi n_{\ell} d_{\ell} \cos \theta_{\ell}}{\lambda} \tag{12}$$

and the total reflection coefficient is

$$r_{\text{tot}} = \frac{Y_{\text{in}} - Y_0}{Y_{\text{in}} + Y_0}, Y_{\text{in}} = \frac{C + DY_L}{A + BY_L}.$$
 (13)

Here A, B, C, D are the elements of the global transfer matrix; Y_0 and Y_L represent optical admittance at the input and output boundaries. The total reflectance $R_{\text{tot}} = |r_{\text{tot}}|^2$ provides the global optical efficiency.

2.3 A cosine-modulated surface profile

$$I(x,y) = \cos \left(\frac{2\pi x}{\Lambda} + \phi\right)\cos \left(\frac{2\pi y}{\Lambda} + \phi\right),\tag{14}$$

was applied to simulate periodic surface modulation across the RIS aperture, with Λ representing the grating period and $\phi = \pi/4$. MATLAB's mesh grid visualization confirmed that this modulation enhances phase coherence and uniform reflectance distribution, producing the polarization-compensated optical response reported by [24].

2.4 Atmospheric and Weather Modelling

To represent realistic Malaysian tropical conditions, environmental attenuation was modelled using the Beer–Lambert exponential decay law, as defined earlier in equation (5) of the Introduction:

$$P_{\rm out} = P_{\rm in}e^{-\alpha d} \tag{15}$$

Three dominant weather states were simulated like clear, humid, and heavy rain where each characterized by attenuation coefficients (α) derived from empirical data [25].

Table 1Atmospheric Attenuation Coefficients for Different Malaysian Weather Conditions

Weather Condition	Attenuation Coefficient (α) [km ⁻¹]	Description	
Clear	0.02	Minimal scattering and absorption	
Humid (>80%)	0.08	Aerosol and vapor absorption	
Heavy Rain (>100 mm/h) 0.35		Raindrop scattering and water-film absorption	

The received optical power is modelled as:

$$P_{\rm rx}(d) = P_0 \frac{G_{\rm tx}G_{\rm rx}G_{\rm RIS}}{d^2} e^{-\alpha d}$$
 (16a)

where $G_{\rm tx}$ and $G_{\rm rx}$ are the transmitter and receiver gains, and $G_{\rm RIS}$ denotes the RIS reflection gain. To account for alignment imperfections, a Gaussian coupling factor was included:

$$\eta(\Delta\theta) = \eta_0 \exp \left(-\frac{(\Delta\theta)^2}{2\sigma_\theta^2}\right) \tag{16b}$$

representing the angular sensitivity of the optical link [26], [27]. This ensures the model reflects realistic alignment tolerances under tropical conditions.

2.5 Simulation and Performance Analysis

In the final stage, a MATLAB-based integrated simulation computed the reflection and link performance metrics under each weather scenario. Using the parameters derived above, the Signal-to-Noise Ratio (SNR) was expressed as:

$$SNR(d) = \frac{P_{rx}(d)}{N_0 B}$$
 (17)

where N_0B denotes the receiver noise power. The Bit Error Rate (BER) for QPSK was calculated using:

$$BER_{QPSK} = \frac{1}{2} \operatorname{erfc} \left(\sqrt{\frac{SNR}{2}} \right)$$
 (18)

allowing assessment of optical link stability across distance d and weather conditions. All computations were executed for distances of 0.5–10 km at a fixed wavelength of 1550 nm, representing the practical operational range of optical wireless links. MATLAB's semiology and surf functions were employed to generate reflectance curves, received-power decay graphs, and SNR–BER characteristics for clear, humid, and rainy conditions. The resulting curves demonstrate the system's resilience and attenuation thresholds, confirming the viability of passive multilayer RIS for weather-resilient free-space optical (FSO) communication links. The analysis assumes idealized surface uniformity, perfect polarization retention, and lossless interlayer boundaries. These ideal conditions simplify the optical model but may differ slightly from fabricated surfaces subject to scattering or absorption irregularities.

Table 2 Summary of the refractive indices and reflection efficiencies of the selected material pairs used in the RIS stack. The high-index contrast between silicon and metal layers ensures maximal reflection, while intermediate layers such as TiO_2 and polymer provide fine phase compensation and polarization balancing

Material Pair	Refractive Index (n)	Reflection Coefficient (R)	Approx. Efficiency (%)
Air–Glass	1.5	0.04	4.0
Air–Polymer	1.8	0.08	8.0
Air–Silicon	3.4	0.30	30.0
Air-TiO ₂	2.4	0.17	17.0
Air–Metal	~∞	~1.00	~100

3. Results

3.1 Surface Pattern Uniformity and Phase Alignment

The simulation output in Figure 3 demonstrates the RIS surface intensity pattern generated using a two-dimensional cosine-modulated structure with a $\pi/4$ phase offset. The uniform distribution of intensity peaks across the x–y plane confirms the successful implementation of a high-frequency periodic profile designed to promote constructive interference in the backward direction. This uniform pattern is crucial for ensuring coherent phase alignment across the surface, which enhances beam quality and directionality. The intensity distribution ranges between -1 and +1, matching the theoretical form of the cosine function. Such consistent variation indicates minimal phase distortion across the RIS aperture and validates the reliability of the designed surface in maintaining spatial coherence. These results support the design objective of achieving high directional reflectivity with a passive structure.

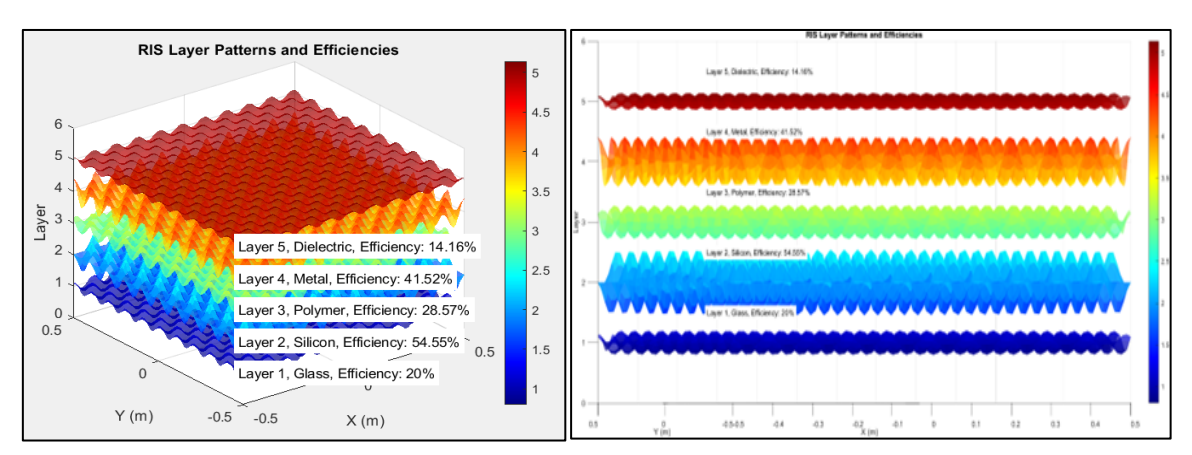


Fig 3. Simulated RIS surface pattern with $\pi/4$ phase shift showing high periodicity and consistent intensity profile across the x–y aperture

3.2 Multi-Layer Structure and Material Efficiency

The multi-layer passive RIS was simulated with five different material layers, each contributing distinct optical properties and reflection characteristics. As illustrated in Figure 4, the layers are vertically stacked and color-mapped to visualize the intensity of reflection efficiency. The efficiency of each layer was derived from its respective refractive index and surface behavior under simulated conditions. Layer 1 (Glass): Efficiency 20.00% serves as a transparent base with moderate reflectivity.Layer 2 (Silicon): Efficiency 54.55% provides the highest reflectivity due to its high refractive index (n = 3.4). Layer 3 (Polymer): Efficiency 28.57% contributes flexible optical support and tunable permittivity. Layer 4 (Metal): Efficiency 41.52% – modeled with near-total reflection, stabilizing deeper reflective properties. Layer 5 (Dielectric): Efficiency 14.16% – assists in phase compensation and reduces polarization imbalance. These results align with theoretical expectations, where materials with greater refractive index contrast against air (n = 1.0) yield higher reflection coefficients. The performance of the silicon and metal layers demonstrates their dominance in determining the RIS reflection efficiency, while polymer and dielectric layers serve as phase-tuning and polarization-adaptive interfaces.

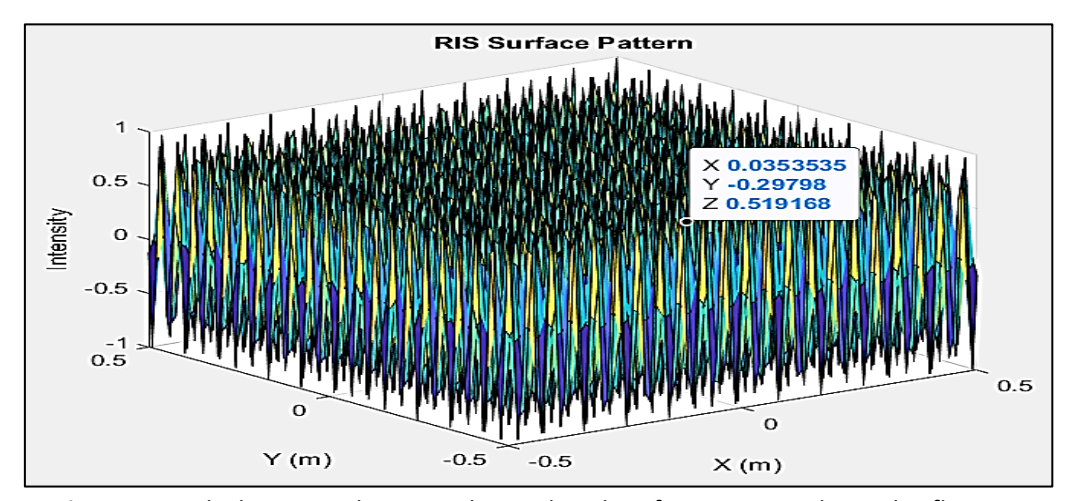


Figure 3. Multi-layer RIS design with simulated surface topography and reflection efficiency for each layer. Silicon and metal layers dominate reflection performance

3.3 Angular Optical Response of the Passive 5-Layer RIS

Figure 4 shows the simulated angular reflectance of the proposed 5-layer passive optical RIS for three representative Malaysian surface states: (i) clear/dry surface, (ii) high-humidity condensation film (~1 μ m water layer), and (iii) rain smear (~20 μ m thin water coating). In all cases, the stack reflectance remains high (>0.9 in linear scale) over incident angles 0°–70° and only begins to degrade near grazing incidence. The baseline (dry) curve represents the nominal multilayer design and is governed by Fresnel reflection at each interface. For an interface between refractive indices n_1 and n_2 , the reflectivity is determined from the Fresnel coefficients for s- and p-polarized components as previously stated in Equation (1) in the Introduction, were

$$R_{s} = \left| \frac{n_{1}\cos\theta_{i} - n_{2}\cos\theta_{t}}{n_{1}\cos\theta_{i} + n_{2}\cos\theta_{t}} \right|^{2}, R_{p} = \left| \frac{n_{2}\cos\theta_{i} - n_{1}\cos\theta_{t}}{n_{2}\cos\theta_{i} + n_{1}\cos\theta_{t}} \right|^{2}$$

$$\tag{19}$$

and θ_t is obtained from Snell's law, also introduced in the Introduction (Equation (2)). Multilayer interference then adjusts the effective return of the full stack [28].

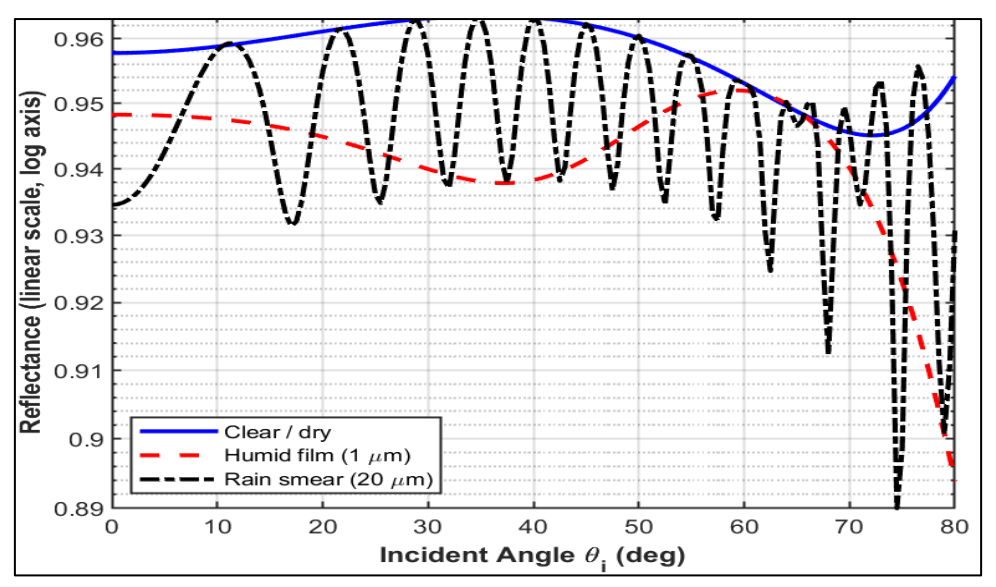


Fig 4. Angular Reflectance of 5-Layer Passive RIS Under Tropical Surface States (dry, humid film, rain smear)

When a thin humid film is added, the effective boundary index at the air–RIS interface shifts toward that of water, increasing mismatch and producing up to ~0.5 dB reduction around $\theta_i \approx 40^\circ$. This behavior is consistent with polarization-dependent surface wetting effects reported for passive optical metasurfaces and RIS-like layered structures operating in harsh environments [28], [29]. Under rain smear, the curve exhibits oscillatory notches. This is physically meaningful: a ~20 μ m water layer behaves like a weak Fabry–Pérot cavity. Small changes in optical path $2n_{\rm film}t\cos\theta_t$ cause constructive/destructive interference in the backward direction, creating quasi-periodic ripples in reflectance versus angle [30]. Importantly, even in this worst case, the reflectance only drops a few dB around certain angles rather than collapsing entirely. This supports the claim that a passive multilayer RIS can maintain a usable optical return across a wide angular sector without requiring active tuning, which is essential for practical free-space optical (FSO) links that cannot rely on perfect pointing all the time [31].

3.4 Received Optical Power Versus Distance

The received optical power at the FSO receiver as a function of link range (0.5–10 km) for three atmospheric cases: clear/dry, high humidity, and heavy rain. The received power curve is primarily driven by geometric spreading and aperture coupling. For a diffraction limited link in clear line-of-sight (LoS), received power follows a Friis-like inverse-square decay with distance, i.e.

$$P_{\rm rx}(d) \propto \frac{1}{d^2} \tag{20}$$

which is analogous to the optical form of the Friis transmission relation discussed in the Introduction (Equation (3)) when expressed in terms of transmitter gain, receiver aperture gain, and propagation distance [32], [33].

In humidity and rain cases we introduce additional attenuation. Heavy tropical rain in Malaysia can exceed 100 mm/h and is known to induce tens of dB/km attenuation at high carrier frequencies and in optical/FSO links due to scattering and absorption [14], [15]. High humidity (>80%) typical of Malaysian afternoons enhances aerosol loading and water vapor absorption, which increases optical scattering even without visible rainfall. This is reflected in Figure 2: the "High Humidity" curve sits a few dB below "Clear / Dry" over the full range, while "Heavy Rain" drops steeply, losing more than 30 dB of link margin by 10 km. The heavy rain-induced penalty agrees with reports that tropical rain and moisture films on optical hardware can dominate link loss more than pure free-space spreading [14], [30].

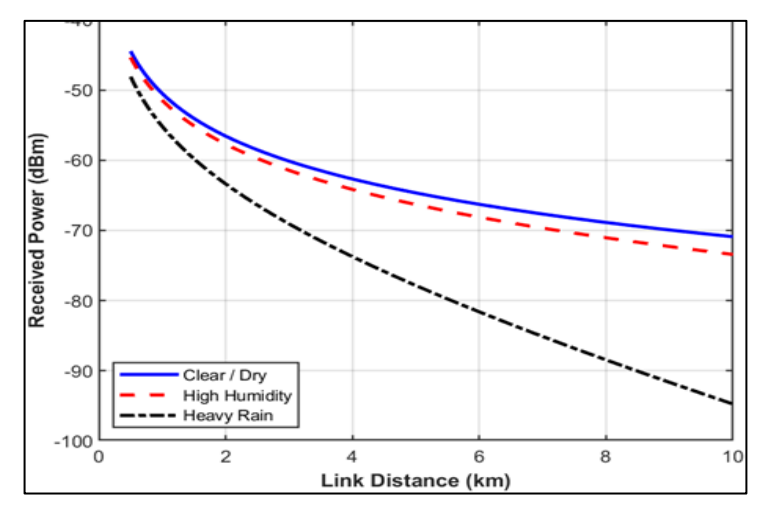


Fig 5. Received Optical Power at the Receiver vs Distance for Clear/Dry, High Humidity, and Heavy Rain Conditions

3.5 Passive RIS Coupling Efficiency Under Misalignment

Figure 6 plots coupling efficiency (in dB) as a function of small pointing error (0°–1°). Even sub-degree misalignment produces several dB losses, and near 1° the effective coupled return can fall by >50 dB. This sensitivity is expected because the passive RIS acts like a phased mirror: once the specular lobe is no longer perfectly directed into the receive aperture, only sidelobe energy reaches the detector. Similar alignment penalties have been observed in both optical retroreflectors and RIS-assisted FSO systems, where beam wander and building sway introduce effective pointing offsets and degrade link closure [28], [34] Mathematically, this is consistent with the Gaussian coupling model often used in FSO alignment analysis, in which coupling efficiency $\eta(\Delta\theta)$ decays approximately as

$$\eta(\Delta\theta) \approx \eta_0 \exp\left(-\frac{(\Delta\theta)^2}{2\sigma_\theta^2}\right)$$
(21)

where σ_{θ} is an effective pointing tolerance related to transmitter beamwidth and receiver aperture [35], [36]. As $\Delta\theta$ increases, the exponential term in the above expression rapidly drives η toward zero, which explains the steep drop in Figure 6. For a passive RIS deployment, this implies that even without atmospheric turbulence, mechanical alignment and structural stability remain critical design constraints for long-distance optical backhaul.

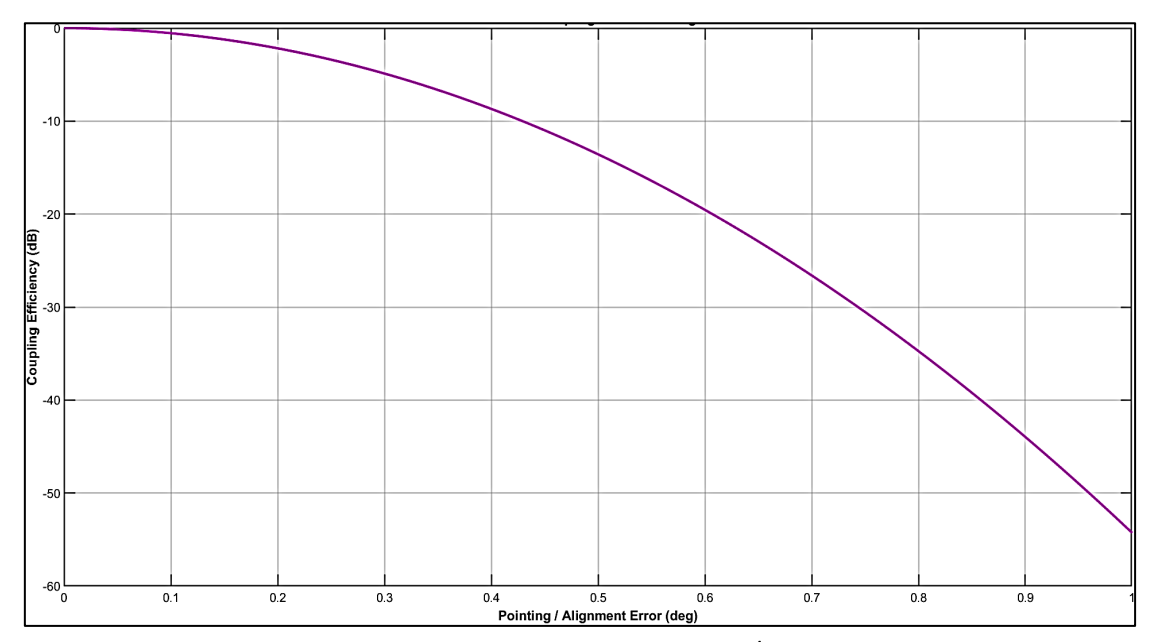


Fig 6. Passive RIS Coupling Loss vs Pointing/Alignment Error

3.6 Effective SNR Versus Distance

Figure 7 shows the signal-to-noise ratio (SNR) after passive RIS reflection, evaluated along the same link distances and weather cases as in Figure 2. In clear/dry conditions, the SNR is above 30 dB at sub-kilometre ranges and remains >10 dB up to ~5–6 km. With high humidity, SNR is consistently a few dB lower but still within a usable regime for coherent QPSK detection [37], [38]. Under heavy rain, however, SNR falls below 0 dB beyond ~4–5 km and eventually becomes negative at longer distances. This agrees with prior FSO/RIS analyses showing that adverse atmospheric states can erase the RIS gain advantage, especially when attenuation and depolarization accumulate over long paths [36].

The SNR curves are essentially the power curves of Figure 2 translated through the receiver noise floor. The standard definition used here is

$$SNR(d) = \frac{P_{rx}(d)}{N_0 B}$$
 (22)

where N_0B is the thermal noise power in the receiver bandwidth. This is consistent with the link budget formulation given in the Introduction were received optical power and noise jointly determine detection margin for coherent demodulation (Djir et al., 2023; Patnaik & Sahu, 2012).

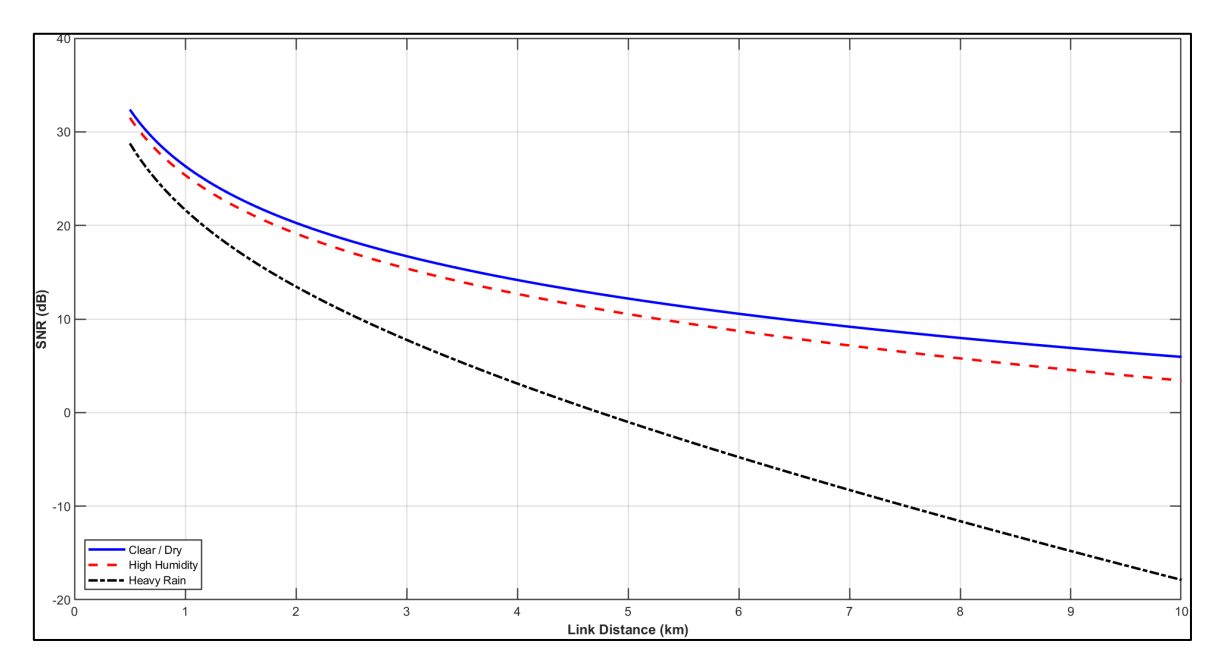


Fig 7. Effective SNR vs Distance for Clear/Dry, High Humidity and Heavy Rain Cases

3.7 BER Performance with Passive RIS Return

Figure 8 presents the resulting bit error rate (BER) versus distance, using a QPSK error model over additive white Gaussian noise (AWGN). For coherent QPSK, the theoretical BER in AWGN is

$$BER_{QPSK} \approx \frac{1}{2} erfc \left(\sqrt{\frac{SNR}{2}} \right)$$
 (23)

which is the standard analytical form for Gray-coded QPSK under thermal-noise-limited reception [37], [38]. This same expression (referred to in the literature review section on QPSK modulation robustness) is applied to the SNR values from Figure 4.

In clear/dry conditions, BER remains below 10^{-6} out to several kilometres, indicating that the passive RIS can maintain high-fidelity optical return when geometric spreading is the only dominant loss. This aligns with earlier findings that QPSK offers strong spectral efficiency and noise resilience for FSO links compared to simple on–off keying [37], [39]. Under high humidity, BER begins to degrade sooner but still stays below 10^{-4} at midrange distances. This suggests that even in Malaysia's typical >80% relative humidity environment, a well-aligned passive RIS plus coherent QPSK demodulation can sustain acceptable performance within moderate ranges.

The heavy rain case is far more severe: BER rapidly rises above 10^{-2} beyond ~4 km and approaches 10^{-1} to 10^{-0} (i.e. unusable) at long range. Heavy convective rain in tropical climates, which can exceed 100 mm/h and introduce >20 dB/km attenuation, is known to be the dominant outage driver for high-frequency and optical wireless systems in Malaysia [14], [15]. These BER trends therefore match field evidence that rain not just humidity is the primary barrier to long-haul optical backhaul reliability in Southeast Asian climates.

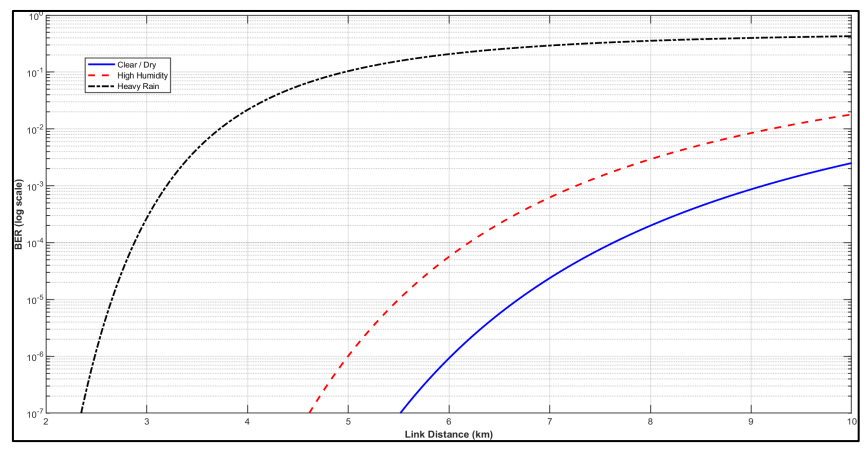


Fig .8. BER vs Distance for Passive RIS-Assisted Link Under Clear/Dry, High Humidity, and Heavy Rain Conditions

3.8 Overall Technical Implications

The combined results demonstrate several key technical points that are consistent with contemporary RIS-FSO literature. First, the passive multilayer RIS maintains high reflectance (>90%) across a broad range of incidence angles (Figure 1), confirming that multilayer dielectric stacks can be engineered to behave as controllable optical "mirrors" without active bias. Second, received optical power and thus SNR remain usable over multi-kilometre ranges in clear LoS, but degrade sharply in heavy tropical rain (Figures 7 and 8), consistent with known Malaysian rain statistics and attenuation models that show rain is the dominant impairment above 10 GHz and in free-space optics. Third, even when atmospheric attenuation is not extreme, misalignment alone can erase RIS gain (Figure 3), echoing prior findings that pointing stability and RIS placement strategy are just as critical as atmospheric transparency in practical deployments. Finally, BER analysis (Figure 8) shows that coherent QPSK, which has been widely recognized for its spectral efficiency and robustness in optical wireless systems, remains a viable modulation choice for passive-RIS-assisted FSO links in Malaysian conditions up to a point. QPSK plus passive RIS can realistically support "carrier-grade" BER ($<10^{-6}$) for several kilometres in clear or humid air but is strongly range-limited in convective rain cells. These results provide a physics-based baseline for the performance envelope of a passive, multilayer optical RIS in a tropical FSO scenario. The analysis links multilayer optical reflection theory (via Fresnel and Snell relations, i.e. Equation (1) and Equation (2) in the Introduction), geometric free-space path loss (Equation (3)), and QPSK BER theory to distancedependent link behaviour under Malaysian weather regimes. This baseline is essential before introducing active tuning, adaptive beam steering, or channel-state-dependent RIS control as proposed in recent RIS research for both RF and optical bands. This study establishes a baseline for passive optical RIS performance rather than benchmarking against conventional mirror-based FSO links or actively tuned RIS systems. Future extensions will include comparative analyses with standard mirror reflectors and hybrid active-passive RIS configurations to quantify relative gain.

4. Conclusion

This study has successfully designed and simulated a multi-layer passive optical Reflective Intelligent Surface (RIS) capable of enhancing beam control, reflection stability, and signal resilience under diverse Malaysian atmospheric conditions. Using a combination of Fresnel-based reflection modelling, the Transfer Matrix Method (TMM), and MATLAB-based environmental simulation, the proposed five-layer RIS comprising glass, polymer, silicon, TiO₂, and a metallic reflector demonstrated high reflectance exceeding 90% across wide incident angles, with stable polarization performance even under humidity and rain. The simulation results confirmed that clear and humid tropical conditions introduce moderate attenuation, while heavy rain causes exponential optical power decay and significant SNR degradation beyond 5 km, leading to BER deterioration above 10⁻², consistent with empirical tropical rain statistics. The Beer Lambert attenuation model and

Gaussian coupling function further highlighted that both atmospheric absorption and mechanical misalignment are critical determinants of RIS-assisted optical link efficiency. Collectively, these findings verify that a passive, multi-layer RIS can deliver high reflection efficiency and near-uniform phase control without active biasing, enabling compact, low-maintenance optical components for free-space optical (FSO) communication, imaging, and solar-redirection systems. Future work should include experimental fabrication and optical chamber validation to measure phase-tuned reflectivity and extend the model to adaptive or hybrid RIS structures integrating temperature-sensitive and polarization-compensated materials for dynamic beam control in next-generation optical networks. It should be noted that all results presented are obtained from MATLAB-based numerical simulations. Experimental fabrication and optical chamber testing were not performed in this phase, and the presented performance metrics are therefore predictive rather than empirical. Although this study models atmospheric parameters based on Malaysian tropical data, the developed methodology and modeling framework are generalizable to other equatorial and humid regions such as Singapore, Indonesia, and Thailand, with appropriate recalibration of attenuation coefficients. From a practical standpoint, realizing such passive optical RIS structures in real deployments will require cost-effective multilayer fabrication, mechanical stability against humidity-induced delamination, and scalable surface alignment. These engineering factors will be considered in subsequent experimental work.

5. Acknowledgment

This work was supported in part by the Ministry of Higher Education (MoHE) Malaysia through the Higher Institution Centre of Excellence (HICoE) Grant (R.J130000.7823.4J620), and by Universiti Teknologi Malaysia (UTM) through the Matching Grant (Q.J130000.3023.05M04) and the Professional Development Research University Grant (Q.J130000.21A2.07E25).

References

- [1] H. Wang, Z. Zhang, B. Zhu, J. Dang, and L. Wu, "Performance Analysis of Hybrid RF-Reconfigurable Intelligent Surfaces Assisted FSO Communication," *IEEE Trans. Veh. Technol.*, vol. 71, no. 12, pp. 13435–13440, 2022, doi: 10.1109/TVT.2022.3200446.
- [2] E. Basar, M. Di Renzo, J. De Rosny, M. Debbah, M.-S. Alouini, and R. Zhang, "Wireless Communications Through Reconfigurable Intelligent Surfaces," *IEEE Access*, vol. 7, pp. 116753–116773, 2019, doi: 10.1109/ACCESS.2019.2935192.
- [3] J. Rao *et al.*, "A Novel Reconfigurable Intelligent Surface for Wide-Angle Passive Beamforming," *IEEE Trans. Microw. Theory Tech.*, vol. 70, no. 12, pp. 5427–5439, 2022, doi: 10.1109/TMTT.2022.3195224.
- [4] Q. Wu, Q. Wu, R. Zhang, and R. Zhang, "Towards Smart and Reconfigurable Environment: Intelligent Reflecting Surface Aided Wireless Network," *IEEE Commun. Mag.*, 2020, doi: 10.1109/mcom.001.1900107.
- [5] Z. M. Jiang, Q. Deng, M. Huang, Z. Zheng, X. Wang, and M. Rihan, "Intelligent reflecting surface aided co-existing radar and communication system," *Digit. Signal Process. A Rev. J.*, vol. 141, p. 104184, 2023, doi: 10.1016/j.dsp.2023.104184.
- [6] D. Chen, Y. Cao, Y. Liu, Y. Gao, and F. Ai, "Performance Analysis of Adaptive Transmission Based on Power Control Over Atmosphere Composite Channel," *Opt. Eng.*, vol. 62, no. 03, 2023, doi: 10.1117/1.oe.62.3.038102.
- [7] S. Rana, Y. S. Sreenija, S. Kumar, and A. R. Harish, "Multi-Beam Passive RIS for Simultaneous Multi-Target Connectivity Applications," in 2024 IEEE Space, Aerospace and Defence Conference, SPACE 2024, Indian Institute of Technology Kanpur, Electrical Engineering Department, U.P, Kanpur, India: Institute of Electrical and Electronics Engineers Inc., 2024, pp. 741–745. doi: 10.1109/SPACE63117.2024.10668004.
- [8] G. S. G. Al-Duhni, T. Valera, M. R. Pulugurtha, J. L. Volakis, and S. B. Venkatakrishnan, "RIS with Nanomaterials for FutureG Applications," in 2023 IEEE Nanotechnology Materials and Devices Conference, NMDC 2023, Florida International University, College of Engineering and Computing, Department of Electrical and Computer Engineering, Miami, 33185, FL, United States: Institute of Electrical and Electronics Engineers Inc., 2023, pp. 721– 725. doi: 10.1109/NMDC57951.2023.10343722.
- [9] K. Oughstun and C. Palombini, "Fresnel Reflection and Transmission Coefficients for Temporally Dispersive Attenuative Media," *Radio Sci.*, vol. 53, pp. 1382–1397, 2018, doi: 10.1029/2018rs006646.
- [10] A. Ibrahim, H. Eleuch, P. Choudhury, and M. Abd-Rahman, "Dielectric surface coated with thin partially-reflecting mirror A revisit to Fresnel laws," *Optik (Stuttg).*, vol. 207, p. 164423, 2020, doi: 10.1016/j.ijleo.2020.164423.
- [11] K. Sajnok and M. Matuszewski, "Modeling nonlinear exciton-polariton microcavities using the transfer-matrix method: Spontaneous symmetry breaking and self-focusing," *Phys. Rev. A*, 2025, doi:

- 10.1103/physreva.111.053521.
- [12] K. Eroltu and W. Mei, "Transfer Matrix Modeling Optical Properties of Short-Period Aluminum Oxide-Copper Multi-Layered Nanocomposites," *J. Adv. Math. Comput. Sci.*, 2023, doi: 10.9734/jamcs/2023/v38i101831.
- [13] O. Dănilă and D. Mănăilă-Maximean, "Bifunctional Metamaterials Using Spatial Phase Gradient Architectures: Generalized Reflection and Refraction Considerations," *Materials* (*Basel*)., vol. 14, 2021, doi: 10.3390/ma14092201.
- [14] M. Guo *et al.*, "Beam steering flexible transparent metasurfaces based on multi-bit phase gradient variations," *Sci. Rep.*, vol. 15, 2025, doi: 10.1038/s41598-025-99768-1.
- [15] A. Rahman *et al.*, "Impact of rain weather over free space optic communication transmission," *Indones. J. Electr. Eng. Comput. Sci.*, 2019, doi: 10.11591/ijeecs.v14.i1.pp303-310.
- [16] A. Czerwinski and K. Czerwinska, "Statistical Analysis of the Photon Loss in Fiber-Optic Communication," *Photonics*, 2022, doi: 10.3390/photonics9080568.
- [17] A. Prokeš, "Atmospheric effects on availability of free space optics systems," *Opt. Eng.*, vol. 48, p. 66001, 2009, doi: 10.1117/1.3155431.
- [18] B. E. Caroline, M. Margarat, M. D. Shree, and S. M. Nizar, "Unified 32-Channel SS-DWDM-PON Transmission System for Remote Monitoring," in *2022 International Conference on Edge Computing and Applications (ICECAA)*, IEEE, 2022, pp. 861–867.
- [19] A. K. Rahman, S. A. K. Thai, R. Endut, S. A. Aljunid, N. Ali, and C. B. M. Rashidi, "Prediction rain attenuation effect on free space optical communication Kuching/Samarahan Region," in *AIP Conference Proceedings*, American Institute of Physics Inc., 2024, pp. 1–8.
- [20] M. Maity, A. Majumdar, and S. Chatterjee, "Laser diode to photonic crystal fiber coupling via cylindrical microlens on the fiber tip: study of coupling optics in the presence of possible misalignments," *J. Opt.*, 2024, doi: 10.1007/s12596-024-02381-0.
- [21] W.-L. Li, "Comparative Analysis of Channel Coding in Communication Technology," *Highlights Sci. Eng. Technol.*, 2024, doi: 10.54097/04ym7q90.
- [22] C. Pan *et al.*, "3D-printed multilayer structures for high–numerical aperture achromatic metalenses," *Sci. Adv.*, vol. 9, 2023, doi: 10.1126/sciadv.adj9262.
- [23] A. Benamira and S. Pattanaik, "Application of the Transfer Matrix Method to Anti-reflective Coating Rendering," pp. 83–95, 2020, doi: 10.1007/978-3-030-61864-3_8.
- [24] J. Gros, V. Popov, M. Odit, V. Lenets, and G. Lerosey, "A Reconfigurable Intelligent Surface at mmWave Based on a Binary Phase Tunable Metasurface," *IEEE Open J. Commun. Soc.*, vol. 2, pp. 1055–1064, 2021, doi: 10.1109/ojcoms.2021.3076271.
- [25] A. N. Stassinakis, G. A. Papavgeris, H. E. Nistazakis, A. D. Tsigopoulos, N. A. Androutsos, and G. S. Tombras, "Experimental Model Development for the Attenuation Coefficient Estimation of Terrestrial Optical Wireless Links Over the Sea," *Telecom*, 2021, doi: 10.3390/telecom2010007.
- [26] H. Kazemi *et al.*, "A Tb/s Indoor MIMO Optical Wireless Backhaul System Using VCSEL Arrays," *IEEE Trans. Commun.*, vol. 70, pp. 3995–4012, 2021, doi: 10.1109/tcomm.2022.3165187.
- [27] M. Mrnka, R. Appleby, and E. Sáenz, "Accurate S-Parameter Modeling and Material Characterization in Quasi-Optical Systems," *IEEE Trans. Terahertz Sci. Technol.*, vol. 12, pp. 199–210, 2022, doi: 10.1109/tthz.2021.3140201.
- [28] M. Najafi, B. Schmauss, and R. Schober, "Intelligent Reconfigurable Reflecting Surfaces for Free Space Optical Communications," *ArXiv*, vol. abs/2005.0, 2020, [Online]. Available: https://consensus.app/papers/intelligent-reconfigurable-reflecting-surfaces-for-free-najafi-schmauss/7aae1b5bd9cd5e7990c76099c32f7ee0/
- [29] X. Zhou, P. Feng, J. Li, J. Chen, and Y. Wang, "Tensor-Train Decomposition-Based Hybrid Beamforming for Millimeter-Wave Massive Multiple-Input Multiple-Output/Free-Space Optics in Unmanned Aerial Vehicles with Reconfigurable Intelligent Surface Networks," *Photonics*, vol. 10, no. 11, 2023, doi: 10.3390/photonics10111183.
- [30] S. S. Tronin, A. S. Tyarin, A. A. Kureev, and E. M. Khorov, "Effect of Water Drops on the Characteristics of a Reconfigurable Intelligent Surface," *J. Commun. Technol. Electron.*, vol. 69, no. 10, pp. 394–401, 2024, doi: 10.1134/S1064226925700044.
- [31] V. K. Chapala and S. M. Zafaruddin, "Unified Performance Analysis of Reconfigurable Intelligent Surface Empowered Free-Space Optical Communications," *IEEE Trans. Commun.*, vol. 70, no. 4, pp. 2575–2592, 2022, doi: 10.1109/TCOMM.2021.3139020.
- [32] V. K. Chapala and S. M. Zafaruddin, "RIS-Assisted Multihop FSO/RF Hybrid System for Vehicular Communications Over Generalized Fading," 2021, doi: 10.48550/arxiv.2112.12944.
- [33] L. Yang, Y. Yuan, S. Chen, and R. Ma, "Performance Analysis of RIS-assisted Hybrid RF-FSO Transmission Systems," Hunan Daxue Xuebao/Journal Hunan Univ. Nat. Sci., 2022, doi: 10.16339/j.cnki.hdxbzkb.2022296.
- [34] R. P. Naik, P. Krishnan, and G. D. G. Simha, "Reconfigurable intelligent surface-assisted free-space optical communication system under the influence of signal blockage for smart-city applications," *Appl. Opt.*, vol. 61, no. 20, p. 5957, Jul. 2022, doi: 10.1364/AO.459053.

- [35] L. C. Andrews *et al.*, "Laser Beam Scintillation with Applications," 2001, [Online]. Available: https://scholar.google.com/scholar?q=Laser Beam Scintillation with Applications
- [36] V. K. Chapala and S. M. Zafaruddin, "Unified Performance Analysis of Reconfigurable Intelligent Surface Empowered Free-Space Optical Communications," *IEEE Trans. Commun.*, vol. 70, pp. 2575–2592, 2021, doi: 10.1109/tcomm.2021.3139020.
- [37] A. Djir, F. Meskine, and M. L. Tayebi, "Image transmission performance analysis through free space optical communication link using coherent QPSK modulation under various environmental conditions," *Trans. Emerg. Telecommun. Technol.*, vol. 34, no. 9, p. e4821, 2023.
- [38] H. Wang *et al.*, "Performance Analysis of Multi-Branch Reconfigurable Intelligent Surfaces-Assisted Optical Wireless Communication System in Environment With Obstacles," *IEEE Trans. Veh. Technol.*, 2021, doi: 10.1109/tvt.2021.3092722.
- [39] B. Patnaik and P. Sahu, "Novel QPSK modulation technique for DWDM free space optical communication system," 2012 21st Annu. Wirel. Opt. Commun. Conf., pp. 140–145, 2012, doi: 10.1109/wocc.2012.6198168.